Clays and Clay Minerals, Vol. 60, No. 1, 76–88, 2012.

EFFECTS OF WEATHERING ON GLAUCONITE: EVIDENCE FROM THE ABU TARTUR PLATEAU, EGYPT

BRIGITTE PESTITSCHEK[1], SUSANNE GIER[1], MAHMOUD ESSA[2], AND HANS KURZWEIL[1]

[1] Department of Geodynamics and Sedimentology, University of Vienna, 1090 Vienna, Austria
[2] Department of Geology, University of Assiut, Assiut 71516, Egypt

Abstract—Recognizing weathering effects is significant for any work carried out on glauconites at the surface. The mineralogy and chemistry of glauconite grains exposed to weathering in a hot arid climate for a maximum of 42 y were studied here. The objective of the study was to find the mineralogical and chemical differences between weathered glauconite from the surface and fresh glauconite from the subsurface.

One specific glauconite-bearing layer at the surface (Layer 16) of the Abu Tartur phosphate mine, located in the Western Desert of Egypt, was studied in detail and compared to a fresh, subsurface glauconitic sandstone from the underground mine.

Even within this single surface layer, the brownish-green glauconite grains vary in color and chemical composition. From top to bottom, the grains show an increase in Fe and K and a decrease in Al and S. In addition, the grains show an internal color zonation caused by variation of Fe and K contents between the center and rim of the grains. The differences in color and chemical composition are even more pronounced between the weathered-glauconite grains from the surface and the fresh glauconite grains from the subsurface which are dark green and enriched in Fe and K.

The clay fractions consisted of mixed-layer glauconite (illite)-smectite, with the surface samples containing more expandable smectite (50%) than the subsurface samples (20%). In the charge-distribution diagram for muscovite-pyrophyllite-celadonite, the weathered glauconites at the surface showed a clear trend from smectitic glauconite at the top to illitic glauconite at the bottom of the layer, whereas the fresh subsurface sample plotted exactly in the glauconite field.

The color, mineralogy, and chemistry indicate that the surface samples were strongly altered by weathering processes and that glauconite transformed progressively into Fe-rich mixed-layer illite-smectite and then into smectites. Weathering can thus completely reverse the glauconitization process. For any chemical and mineralogical characterization of glauconites at the surface, these weathering effects must be taken into consideration.

Key Words—Abu Tartur Mine, Egypt, Glauconite, Smectite, Weathering.

INTRODUCTION

Studies of the nature, origin, and genesis of glauconite are numerous (Burst, 1958a, 1958b; Hower, 1961; Ehlmann *et al.*, 1963; Odom, 1976; Velde, 1976; Odin and Matter, 1981; Ireland *et al.*, 1983; Odin, 1988; Chamley, 1989; Strickler and Ferrell, 1990; Geptner and Ivanovskaya, 2000; Meunier, 2004, Meunier and El Albani, 2007). Considerably fewer studies, however, have focused on the weathering products of glauconite (Wolff, 1967; Loveland, 1981; Fanning *et al.*, 1989; Meunier, 2004). Glauconite weathering results in pseudomorphs of goethite and authigenic kaolinite (Wolff, 1967) and ferruginous illite-smectite (Loveland, 1981). Weathering is accompanied by loss of K and Mg, an increase in Al, and considerable grain disaggregation (Loveland, 1981). Fanning *et al.* (1989) studied glauconites from the oxidized and reduced zone of soil-geologic columns and found that glauconite in reduced zones had a greater proportion of its structural Fe in the ferrous state.

According to Odin and Matter (1981), glauconites are mixed-layer minerals consisting of smectite and glauconitic mica. They are K-rich dioctahedral phyllosilicates that generally appear in the form of rounded grains. The two end members are glauconitic mica, an Fe- and K-rich 10 Å illite-type mineral with characteristics of evolved glauconite (Fe_2O_3 > 20%, K_2O > 4%), and glauconitic smectite which forms a mixed-layered mineral group consisting of varying proportions of smectitic-, glauconitic-, and sometimes illitic-type layers (Bailey *et al.*, 1979; Chamley, 1989).

In the present study the effects of weathering on glauconite were studied on samples of the Abu Tartur phosphate mine, located 650 km southwest of Cairo and 50 km west of El Kharga City, Egypt, in the Western Desert (Figure 1). The sediments in the mine are Upper Cretaceous (Campanian–Maastrichtian) phosphorites, black shales, and glauconitic sandstones belonging to the widespread shallow-marine deposits of the Duwi

* E-mail address of corresponding author:
susanne.gier@univie.ac.at
DOI: 10.1346/CCMN.2012.0600107

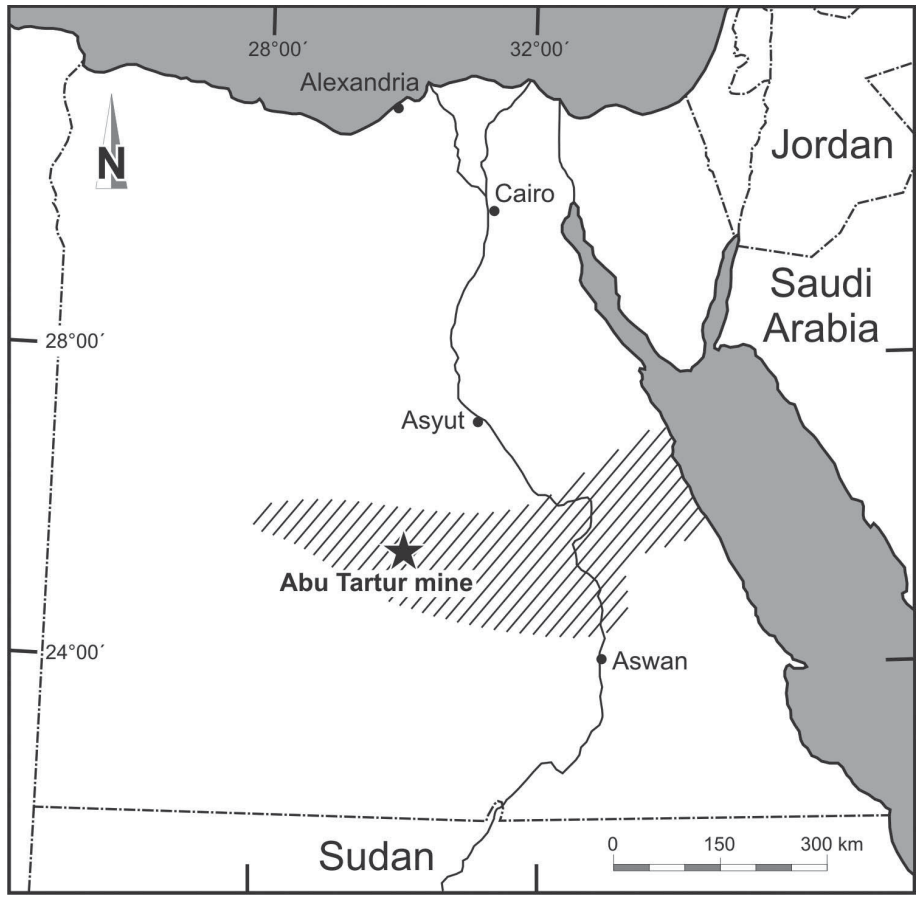

Figure 1. Map of Egypt and the location of the Abu Tartur mine. The extent of the Nile Valley facies is highlighted (Issawi, 1972).

Formation (Sediek and Amer, 2001). The Abu Tartur Plateau has attracted the attention of geologists since the discovery of economically significant phosphate deposits in the Duwi Formation in 1967 (Notholt, 1985; Sediek and Amer, 2001). Both open-pit and underground mining for phosphates are currently active.

The objectives of the present study were twofold. The mineralogy and geochemistry of glauconite grains within one specific layer of a measured section, Layer 16, were analyzed in detail. These surface samples were compared to fresh glauconitic samples from the subsurface in the underground mine to obtain information about the weathering processes.

GEOLOGICAL SETTING

The Upper Cretaceous–Palaeogene sedimentary rocks in central and southern Egypt are characterized by a gradual facies differentiation into three main types (Issawi, 1972): Nile Valley, Garra El-Arbain, and Farafra. These facies are present in three different basins on the northern flank of the African shield. The basins are delineated by exhumed pre-Late Cretaceous undulating surfaces. The Nile Valley facies extends from the Red Sea Coast in the east to Kharga Oasis in the west (Figure 1). The Abu Tartur plateau is located in the Nile Valley facies (Issawi, 1972). The rocks of the Nile Valley facies have been differentiated into several units, from the base to the top: the Nubia (Taref Sandstone and Variegated (= Quseir) Shale members), Duwi, Dakhla, Tarawan, Esna, and Thebes Formations (Issawi, 1972). The Western Desert sequence along the Abu Tartur plateau represents sediments that were confined by a pre-existing depression enclosed by the Dakhla (northwest) and Kharga (southeast) uplifts (Wassef, 1977; Van Houten *et al.*, 1984). With few exceptions these sediments were deposited in shallow epeiric seas which flanked the southern margin of the Tethyan trough. The sediments were deposited in a generally east–west trending belt spanning the middle latitudes of Egypt (Glenn and Arthur, 1990).

Lithologically, the Duwi Formation consists of phosphate beds interbedded with black and gray claystone, sandstone, siltstone, and glauconite beds (Sediek and Amer, 2001). The glauconitic sandstones of the Duwi Formation studied are of Late Campanian to

earliest Maastrichtian age. The Duwi Formation represents the first onset of fully marine conditions in Egypt accompanying the major Late Cretaceous marine transgression of this region.

The strata overlie Lower to Middle Campanian marginal-marine to shallow-marine shales of the (Quseir) Variegated Shale member (also known as the Mut Formation; Said, 1962; Klitzsch *et al.*, 1979; Ward and McDonald, 1979; Hendriks *et al.*, 1984, Van Houten *et al.*, 1984) and underlie deeper-water marine marls and chalks of the Maastrichtian Dakhla Formation (Said, 1962; Mansour and Khallaf, 1979; Mansour *et al.*, 1979; Hendriks *et al.*, 1984; Soliman *et al.*, 1986). The contact between the Duwi and Dakhla formations marks the Campanian-Maastrichtian boundary and is dated at ~71 Ma (Tantawy *et al.*, 2001).

MATERIALS AND METHODS

During fieldwork in spring 2009, the ATM (Abu Tartur Middle, Figure 2) section was measured, logged, sampled, and characterized sedimentologically. The section was taken along a SW–NE striking cliff face in the Abu Tartur mine of Egypt, at N 25º25′36.2″ and E30º05′11.2″. Thirty-six sediment layers could be distinguished, starting with massive black shales at the base, followed by interbeddings of phosphate, glauconite, and black shale layers, and ending with lightly colored sandstones on top of the section. Each layer was investigated macroscopically, and the lithology, grain size, color, and thickness were described in detail.

To study the influences of weathering on glauconites at the surface, a layer from the middle of the studied section (Layer 16, Figure 2) was selected and sampled in detail. The layer is ~80 cm thick; samples AT31–AT36 were taken every 10 to 15 cm in a vertical sequence (Figure 3).

To compare the glauconites from the surface with fresh glauconites, samples from the gallery of the active underground mine were collected. A striking difference in color was noticed immediately between the fresh and weathered hand specimens. The fresh sample was dark green whereas the weathered samples were olive-green to yellowish-brownish green. The entrance to the mine is located at N 25º24′42.72″ and E30º04′32.70″, 60 m below the level of surface Layer 16. The fresh glauconites probably do not belong to the same layer as the weathered ones, but the analyses demonstrated that the original mineralogical composition was the same.

Thin-section microscopy

Standard thin sections were prepared to study the petrology of the glauconitic sandstones (AT31–AT36 and mine) and investigated using a polarizing microscope.

X-ray diffraction

X-ray diffraction (XRD) was used to determine the mineralogical composition of the bulk and the <2 μm samples. All measurements were carried out using a PANalytical X'Pert Pro diffractometer (CuKα radiation

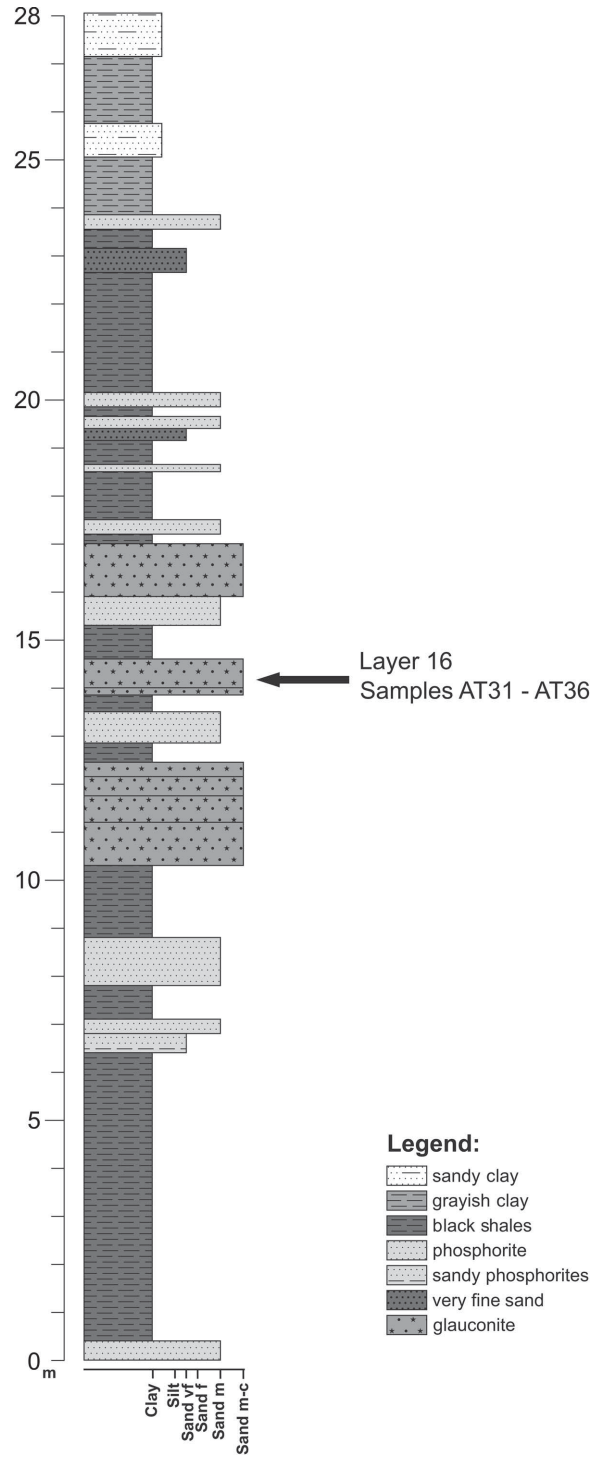

Figure 2. The ATM (Abu Tartur) section consists of black shales, phosphorites, glauconitic sandstones, and (sandy) claystone layers; the position of glauconite Layer 16 (samples AT31–AT36) is shown.

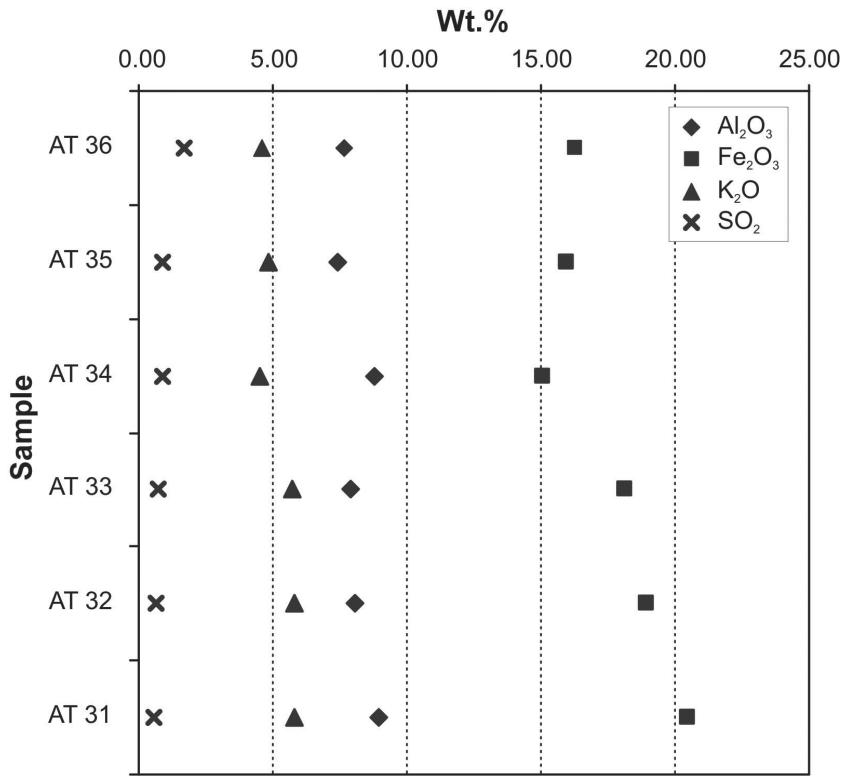

Figure 3. Chemical variations of glauconite grains in surface Layer 16; mean Al_2O_3, Fe_2O_3, K_2O, and SO_2 contents (mean of 14 analyses per sample) of glauconite grains from samples AT31 (base) to sample AT36 (top of Layer 16).

(40 kV, 40 mA), step size = 0.0167, 5 s per step) at the University of Vienna.

Clay-mineral analyses

The clay (<2 μm) fractions of the glauconitic sandstones were obtained according to Moore and Reynolds (1997). For Mg and K saturation, 50 mg of each sample was saturated with $MgCl_2$ and KCl solutions (suspension 1 mg/mL), respectively. After shaking overnight, the suspensions were centrifuged and washed. The suspensions (8 mg/mL) were applied to glass slides, air dried, and analyzed. The Mg-saturated samples were further saturated with glycerol (Gly) and the K-saturated samples with ethylene-glycol (EG) to differentiate between smectite and vermiculite. The samples were heated to 550ºC and further analyzed.

X-ray diffraction patterns were evaluated after Moore and Reynolds (1997) and Brindley and Brown (1980). The percentage of illite (glauconite) in the mixed-layer mineral illite (glauconite)-smectite was determined by the difference in diffraction angles (º2θ) of the mixed-layer peak positions 001/002 and 002/003 of the EG-solvated samples (Moore and Reynolds, 1997).

Random powder specimens of the samples were prepared to determine the d_{060} reflection which allowed the distinction between dioctahedral and trioctahedral minerals, based on the value of the *b* parameter (Brindley and Brown, 1980; Moore and Reynolds, 1997).

X-ray fluorescence (XRF)

For preparation, the samples were heated at 1050ºC in an oven for 120 min to determine the LOI (loss on ignition). Then, 0.55 g of the powdered sample, 5.5 g of flux (Spectromelt A12), and 800 mg of ammonium bromide (to allow removal from the lid) were mixed together and melted in a Pt/Au crucible, producing a glass-like bead.

The beads were measured using an Axios (Technische Prüfanstalt, Vienna) sequential high power X-ray fluorescence spectrometer (Dual-Multi-Channel-Analyzer, 20−60 kV, 10−100 mA).

Electron microprobe (EMP)

The quantitative chemical analyses of the glauconite grains were carried out with a CAMECA SX-100 microprobe (HV: 15 kV, IBeam: 20 nA), equipped with four wavelength-dispersive (WDX) and one energy-dispersive (EDX) spectrometers at the University of Vienna. The thin sections were coated with carbon before analysis.

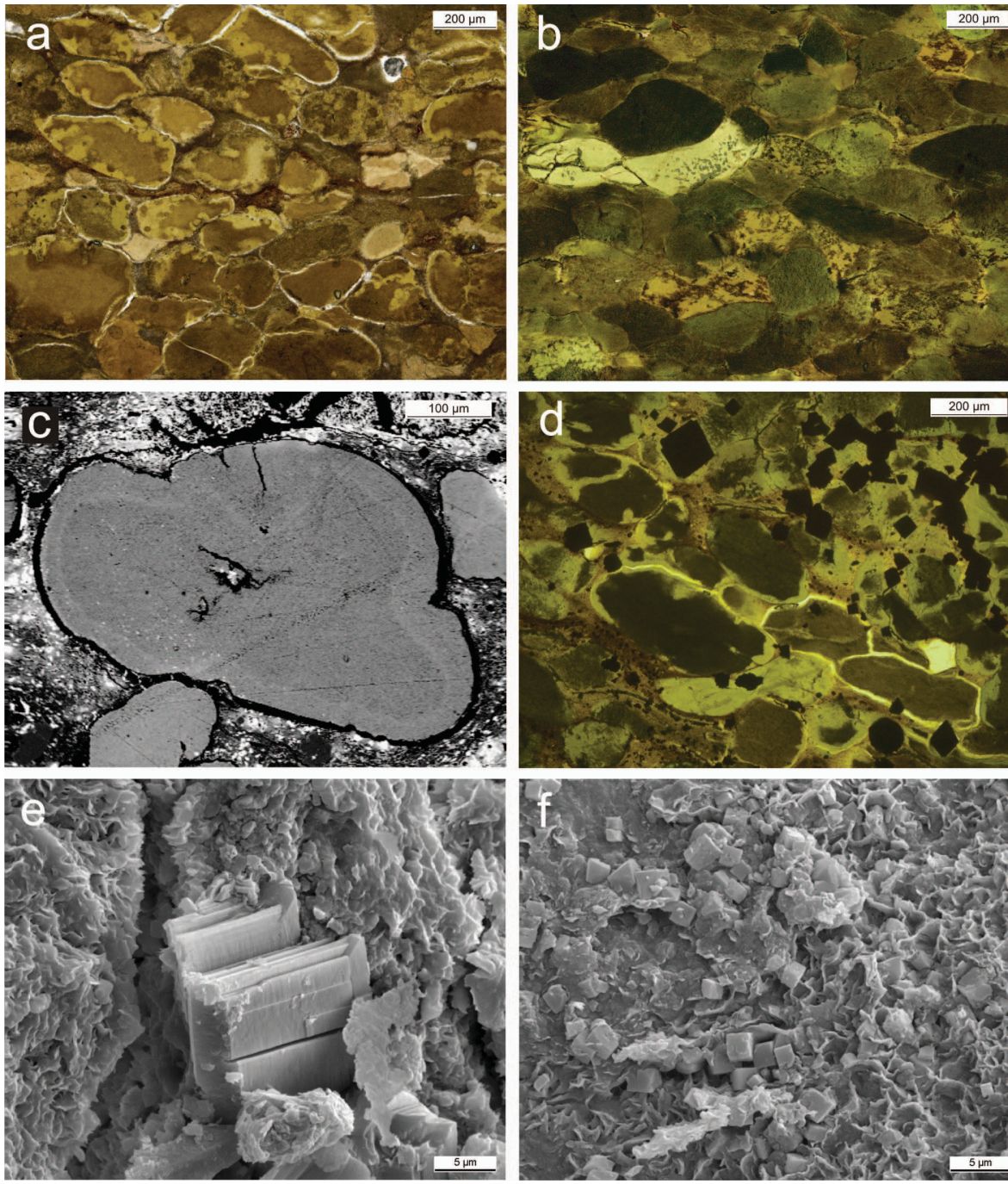

Figure 4. (a) Photomicrograph of a weathered sample AT34 from the surface showing glauconite grains with dark-green to brown central zones, outer zones in different colors and shrinkage structures, PPL (plane polarized light). (b) Photomicrograph of light- to dark-green glauconite grains of the fresh subsurface sample (PPL). (c) BSE image of a zoned surface glauconite grain, AT31. (d) Cubic pyrite crystals (black) in a subsurface sample. (e) Gypsum/anhydrite crystals on a glauconite surface, surface sample AT32. (f) Glauconite grain with cubic pyrite on the surface; surface sample AT36; note the rosette structure of glauconite grain surface (mixed-layer glauconite-smectite).

Scanning electron microscope (SEM)

The scanning electron microscope was used to investigate the morphology and surface of the glauconite grains and to detect possible weathering minerals. The images were made with LEO 1450 EP equipped with an energy dispersive X-ray spectrometer. The cubic

samples (~1 cm × 1 cm × 1 cm) were coated with a film of gold to allow conductivity at the surface and to avoid charging of the samples.

RESULTS

Mineralogy and petrology of the glauconitic sandstones

Based on optical microscopy, both surface and mine samples can be classified as glauconitic sandstones to glauconitic wackes (Figure 4a,b) (Pettijohn *et al.*, 1987). The framework grains are predominantly glauconite grains with trace amounts of fine-grained quartz grains. The glauconite grains range in size from 100 to 500 μm. The sandstone samples are well to moderately sorted, well rounded, and grain supported. The grains show point-, long-, and concavo-convex contacts. The main glauconite morphologies are ovoidal, spheroidal, or lobate (Figure 4).

Glauconite exhibited an intense green or brownish-green color in plane polarized light. The grains were aggregates of many small crystals (Figure 4a,b). Glauconite has a moderate birefringence, but interference colors are difficult to observe because they are masked by the intense natural color of the mineral.

The framework grains of the weathered samples from the surface (Figure 4a, sample AT34) were brownish-green in color and were surrounded by a brownish argillaceous matrix. Most grains showed differences in color between the center and outer zones, the outer zones generally being lighter in color. This observation was not grain-size dependent. Both the glauconite grains and the matrix of the surface samples were cut by small, gypsum-cemented fractures. In comparison, the fresh subsurface sample (Figure 4b) consisted of light- to dark-green glauconite grains; grain-zonation was observed but was not as extensive as in the surface samples. The fresh sample contained less matrix than the weathered ones.

Observation by polarizing and scanning electron microscopes revealed that grains of both weathered and fresh samples are often associated with cubic framboidal pyrite crystals on the surface and in the fractures of the grains (Figure 4d,f). The pyrite crystals ranged in size from 1 μm (Figure 4f) to 100 μm (Figure 4d). Pyrite also occurred as pore-filling cement between the glauconite grains and the matrix. Accumulations of octahedral pyrite crystals were often found in shrinkage structures but, in total, pyrite occurred only as a minor constituent. The SEM images of weathered samples AT32 (Figure 4e) and AT35 also showed crystals of gypsum or anhydrite. The surfaces of the grains showed a rosette morphology – the characteristic crystal habit of mixed-layer glauconite-smectite minerals (Figure 4e,f). Precise identification of the mixed-layer mineral was based on XRD and EMP analysis. In summary, the fresh subsurface samples consisted of glauconite, quartz, and pyrite as observed using the optical microsope and in terms of XRD analysis. The surface samples showed, besides glauconite, quartz, and pyrite as in the fresh sample, the presence of weathering minerals such as anhydrite, gypsum, hematite (AT31), and jarosite (AT32–AT36).

Mineralogy of clay fraction

A clay-mineral analysis was carried out on the <2 μm fractions of all samples. As the <2 μm fractions contained matrix and grains, the XRD patterns showed a mixture of both. The XRD patterns of the weathered sample (AT31) from the surface and the fresh subsurface sample with different saturations (EG, Mg, K, Mg+Gly, and K+EG) (Figures 5a and 5b, respectively) showed differences from the XRD pattern of pure glauconite in an oriented sample. According to Brindley and Brown (1980) and Moore and Reynolds (1997) the peak positions of pure glauconite are 10.16 Å (001), 5.01 Å (002) (very weak to non-existent), and 3.38 Å (003) and should be unaffected by saturation with ethylene glycol or glycerol. The shifts of the peak positions revealed that the fresh subsurface sample (Figure 5b) was not 100% glauconite. The peaks of the Mg-saturated sample shifted after solvation with glycerol from 11.38 to 9.56 Å and the K-saturated sample after treatment with ethylene glycol from 10.46 to 9.94 Å. According to Moore and Reynolds (1997), the expandable phase was smectite. In addition, a peak of an ordered mixed-layer mineral with a position at 33.3 Å was observable in the K+EG-saturated sample (Figure 5b). From the $^{o}\Delta 2\theta$ values of the mixed-layer positions 001/002 at 9.50 Å ($9.30^{o}2\theta$) and 002/003 at 5.20 Å ($17.00^{o}2\theta$) of the ethylene glycol-treated sample (EG) (Figure 5b), a glauconite content of 75–80% ($7.70^{o}\Delta 2\theta$) was determined (Brindley and Brown, 1980).

Compared to the fresh subsurface sample, the weathered sample AT31 from the surface (Figure 5a) was more smectitic. The peak position of the Mg-saturated sample shifted from 15.03 to 16.65 Å after solvation with glycerol and of the K saturated sample from 11.38 to 17.02 Å after treatment with ethylene glycol. According to the $^{o}\Delta 2\theta$ value of the mixed-layer positions 001/002 at 9.45 Å ($9.34^{o}2\theta$) and 002/003 at 5.59 Å ($15.83^{o}2\theta$) of the ethylene glycol-treated sample (EG) (Figure 5a), the smectite content of the randomly interstratified mixed-layer glauconite (illite)-smectite was 50% ($6.49^{o}\Delta 2\theta$; Moore and Reynolds, 1997). In comparison, the weathered samples contained more expandable smectite layers in the mixed-layer mineral than the fresh sample (~20%).

The d_{060} reflections gave values of 1.507 Å for the surface and 1.510 Å for the subsurface glauconites, values which are typical of dioctahedral minerals (Odom, 1976).

Chemical composition of the bulk samples

Chemical analyses of the surface bulk samples gave the following minimum to maximum contents:

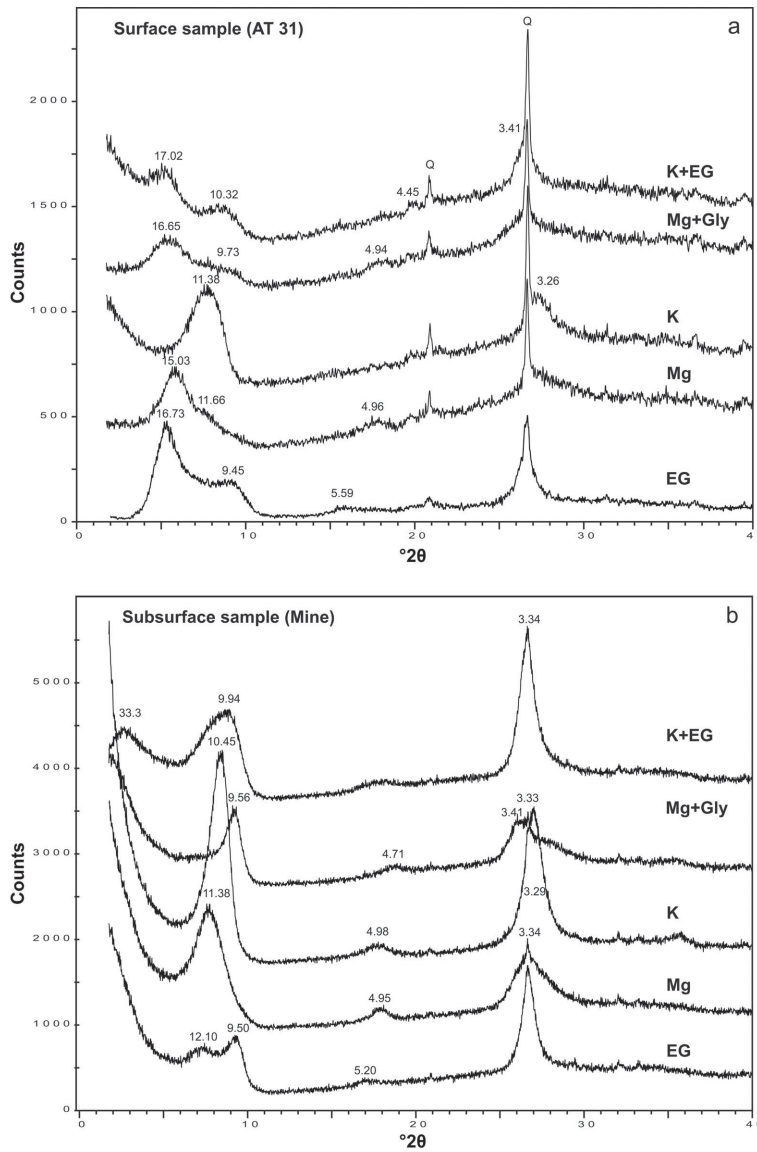

Figure 5. XRD patterns of the clay fraction of: (a) weathered sample AT31 from the surface and (b) fresh subsurface sample. The samples were saturated with ethylene glycol (EG), magnesium (Mg), magnesium plus glycerol (Mg+Gly), potassium (K), and potassium plus ethylene glycol (K+EG). Q = quartz; inserted values are *d* spacings in Å.

40.35–60.76% SiO_2, 6.41–8.72% Al_2O_3, 21.29–43.17% Fe_2O_3, 2.58–3.93% MgO, 2.76–5.50% K_2O, 0.05–2.89% CaO, 0.37–1.53% P_2O_5, and 0.23–0.70% SO_2. The amount of SO_2 in the surface samples is greater because of the presence of anhydrite/gypsum. The chemical composition of the fresh subsurface sample fell within these ranges (55.61% SiO_2, 7.86% Al_2O_3, 22.39% Fe_2O_3, and 3.04% MgO). The K_2O content, an indicator of glauconitization, was 6.19% which is greater than in the weathered samples from the surface. Values of 3.20% CaO and 1.81% P_2O_5 point to an admixture of phosphate minerals (apatite), as the SO_2 content (0.024%) was rather small. Loss on ignition (LOI) values for the weathered samples from the surface were 17.22–25.75% and only 9.28% for the fresh subsurface sample.

Chemical composition and structural formulae of glauconite grains

Electron microprobe analysis was carried out on fresh and weathered samples. Seven morphologically different grains of each sample were analyzed, and the analysis of one representative grain per sample is reported in Table 1. The major elements (wt.%) were measured in the centers and in the outer rims of the glauconite grains. Most of the grains were zoned (Figure 4c). Chemical zonations between the center and the rim of the grains were most pronounced for Al_2O_3, Fe_2O_3, K_2O, and SO_2

Table 1. Representative chemical compositions (wt.%) and structural formulae of the glauconites from the Abu Tartur mine.

	AT 31 Core	AT 31 outer rim	AT 32 core	AT 32 outer rim	AT 33 core	AT 33 outer rim	AT 34 core	AT 34 outer rim	AT 35 core	AT 35 outer rim	AT 36 core	AT 36 outer rim	Mine core	Mine outer rim
SiO_2	49.761	49.451	51.134	50.323	51.624	53.213	52.382	51.644	52.716	53.004	52.571	51.141	53.255	51.519
Al_2O_3	8.125	9.026	8.580	9.174	7.968	8.126	7.611	9.184	7.972	7.783	7.518	6.775	7.303	7.429
Fe_2O_3	21.097	21.483	19.538	18.284	16.842	17.729	15.038	14.014	16.344	16.682	17.517	16.759	20.611	19.616
MnO	0.002	0.019	0.011	0.015	0.010	0.012	0.012	0.015	0.010	0.010	0.010	0.013	0.009	0.015
MgO	3.330	3.377	3.368	3.429	3.114	3.326	2.903	3.136	3.516	3.516	3.569	3.555	2.957	2.853
CaO	0.048	0.069	0.064	0.153	0.202	0.120	0.306	0.312	0.048	0.040	0.143	0.046	0.479	0.443
Na_2O	0.016	0.028	0.006	0.009	0.022	0.008	0.010	0.014	0.014	0.017	0.016	0.006	0.037	0.042
K_2O	5.932	5.594	5.969	5.518	5.344	5.652	4.564	4.093	5.063	5.209	5.100	4.753	6.494	6.298
TiO_2	0.040	0.023	0.048	0.063	0.031	0.036	0.046	0.029	0.048	0.032	0.041	0.031	0.057	0.043
SO_2	0.524	0.833	0.521	0.534	0.346	1.205	0.148	0.230	1.437	1.149	1.465	1.403	0.130	0.047
P_2O_5	0.527	0.630	0.410	0.469	0.428	0.465	0.273	0.262	0.303	0.311	0.301	0.278	0.040	0.025
Total	89.400	90.533	88.813	89.002	85.930	89.892	83.294	82.933	87.470	87.750	88.252	84.760	91.371	88.327
Unit-cell contents based on $O_{10}(OH)_2$														
Tetrahedal														
Si	3.736	3.680	3.790	3.783	3.926	3.915	4.036	3.973	3.958	3.960	3.935	3.974	3.859	3.852
Al	0.264	0.320	0.210	0.217	0.074	0.085		0.027	0.042	0.040	0.065	0.026	0.141	0.148
Charge	−0.264	−0.320	−0.210	−0.217	−0.074	−0.085	0.144	−0.027	−0.042	−0.040	−0.065	−0.026	−0.141	−0.148
Octahedral														
Al	0.455	0.472	0.540	0.596	0.640	0.620	0.691	0.806	0.663	0.645	0.598	0.594	0.483	0.507
Fe^{3+}	1.192	1.203	1.090	1.034	0.964	0.982	0.872	0.811	0.923	0.938	0.987	0.980	1.124	1.104
Mg	0.373	0.375	0.372	0.384	0.353	0.365	0.333	0.360	0.393	0.392	0.398	0.412	0.319	0.318
charge	−0.313	−0.225	−0.366	−0.342	−0.482	−0.464	−0.645	−0.429	−0.456	−0.467	−0.449	−0.454	−0.541	−0.531
Interlayer														
K	0.568	0.531	0.564	0.529	0.519	0.530	0.449	0.402	0.485	0.497	0.487	0.471	0.600	0.601
Na	0.002	0.004	0.001	0.001	0.003	0.001	0.002	0.002	0.002	0.002	0.002	0.001	0.005	0.006
Ca	0.004	0.006	0.005	0.012	0.016	0.009	0.025	0.026	0.004	0.003	0.011	0.004	0.037	0.035
charge	0.578	0.547	0.575	0.554	0.554	0.549	0.501	0.456	0.495	0.505	0.511	0.480	0.679	0.677

(Table 1). The chemical compositions of the glauconite grains obtained by EMP varied within surface Layer 16 (Figure 3); the values are the means of 14 analyses (core and rim analyses of seven grains per sample).

Generally, the glauconite grains from the upper part of surface Layer 16 contained less K_2O than grains from the lower part (Figure 3). The silica content was greater in grains from the upper part of the layer (50.63−55.15% SiO_2). Intermediate silica contents of 48.31−53.96% were found in the fresh subsurface sample.

The Al_2O_3 content of the glauconite grains varied between 6.59 and 11.69%. The results are in good agreement with published aluminum contents obtained by Odin and Matter (1981).

The Fe content of grains from the lower part of surface Layer 16 varied from 16.35 to 24.28% Fe_2O_3. The Fe contents of the fresh subsurface sample varied within a similar range (16.59−22.11% Fe_2O_3). The upper samples of Layer 16 had lower Fe values of 14.01−17.52% Fe_2O_3. The Fe_2O_3 content of the glauconite grains increased towards the lower part of surface Layer 16 (Figure 3).

Potassium increased within surface Layer 16 from the top (4.09−5.23% K_2O) to the bottom (4.44−6.91% K_2O). The fresh subsurface sample had K contents between 5.36 and 7.24% K_2O.

The S content decreased within surface Layer 16 from the top (0.23−2.08% SO_2) to the bottom (0.27−1.40% SO_2) (Figure 3). The S contents of glauconite grains of the fresh subsurface sample were very low, between 0.024 and 0.130% SO_2.

Zonations in color within the glauconite grains were mostly caused by differences in the Fe and K contents. Generally, surface and subsurface grains contained more K, Fe, and Si in the center of the grains with an enrichment of Al in the outer rim. The glauconite grains from the weathered surface layer contained more S in the outer rim.

The FeO contents of the samples were determined from the d_{060} spacings obtained by XRD (Odom, 1976). The 1.507 Å spacing for the surface sample is typical of glauconites with FeO contents of <1 wt.%, the spacing of 1.510 Å for the fresh subsurface glauconite for contents of 2 wt.% FeO (Odom, 1976).

The crystal-chemical structural formulae of 2:1 phyllosilicates were calculated (Table 1; only selected samples reported) using the Marshall Method (Marshall, 1949) and assuming an ideal structure with 22 negative

charges of ten oxygen and two hydroxyl groups (Köster, 1977). An example of a calculated, simplified structural formula for a weathered-glauconite from the surface (sample AT31) is:

$$(K_{0.52}Na_{0.01}Ca_{0.01})(Al_{0.42}Fe_{1.28}Mg_{0.38})(Si_{3.62}Al_{0.38})O_{10}(OH)_2.$$

The Fe contributes more than half of the octahedral charge (Odin and Matter, 1981).

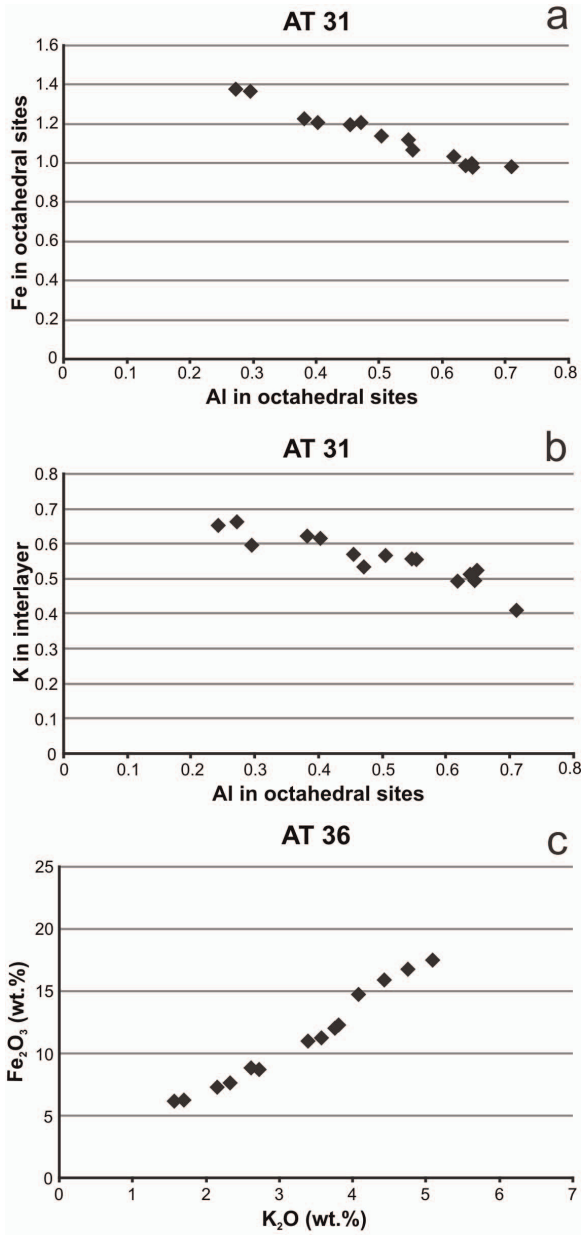

Figure 6. (a) Relationship between Al and Fe in octahedral sites, surface sample AT31; (b) relationship between Al in octahedral sites and K in interlayer position, surface sample AT31; (c) relationship between K_2O and Fe_2O_3 of surface-sample AT36.

The relationships between the main cations (Fe, K, Al) in octahedral and interlayer positions are shown in scatter plots (Figure 6). The major chemical variation in the octahedral sheet of glauconite was the ratio of Al to Fe(III). All samples showed that Al in octahedral sites and Fe(III) in octahedral sites were negatively correlated (Figure 6a); Al increased as Fe(III) decreased. This shows the progressive loss of Fe for octahedral Al during weathering. A negative correlation between Al in octahedral and K in interlayer position was also observed (Figure 6b). The amount of K in the interlayer position of glauconite decreased systematically with an increase of Al in the octahedral sites. The loss of both Fe and K during weathering was demonstrated by the positive correlations between K_2O and Fe_2O_3 (Figure 6c). This shows a reversal of diagenesis, because during diagenesis Fe_2O_3 and K_2O are incorporated into the smectite structure of glauconite (Bornhold and Giresse, 1985; Strickler and Ferrell, 1990; Amorosi, 1997). All these variations in composition of individual glauconite grains were found between different surface samples, and also within a single sample (*e.g.* sample AT31 or AT36 in Figure 6a–c), leading to the conclusion that even within a single sample the majority of the glauconite grains are in different stages of evolution.

In addition, the tetrahedral, octahedral, and interlayer charges were calculated and plotted in a charge-distribution diagram (after Köster, 1977, Figure 7). The charge-plot of weathered samples AT31–AT36 from the surface shows a significant trend from the illite (glauconite) to the montmorillonite (smectite) field. Most of the samples plotted between the smectite field and the illite (glauconite) field, indicating mixed-layer minerals. Two exceptions were observed in sample AT31 from the bottom of the surface layer, which plotted in the illite field. Data of the fresh subsurface sample plotted exactly in the glauconite field. Surface samples AT34–AT36 from the top of the layer plotted in the montmorillonite field.

Generally, the tetrahedral charge increased from sample AT36 to AT31 (top to bottom of the surface layer) while the octahedral charge decreased from AT36 to AT31.

DISCUSSION

Chemical and mineralogical variations of glauconite grains within surface Layer 16

The glauconite grains within Layer 16 (Figures 3, 4) varied in color and in terms of their chemical composition. The colors ranged from light and dark green to yellowish and brownish. The K and Fe increased within individual glauconite grains from the top (AT36) to the bottom (AT31) of surface Layer 16. In contrast, S decreased from the top (AT36) to the base (AT31) within the grains (Figure 3). The lower K and Fe contents in

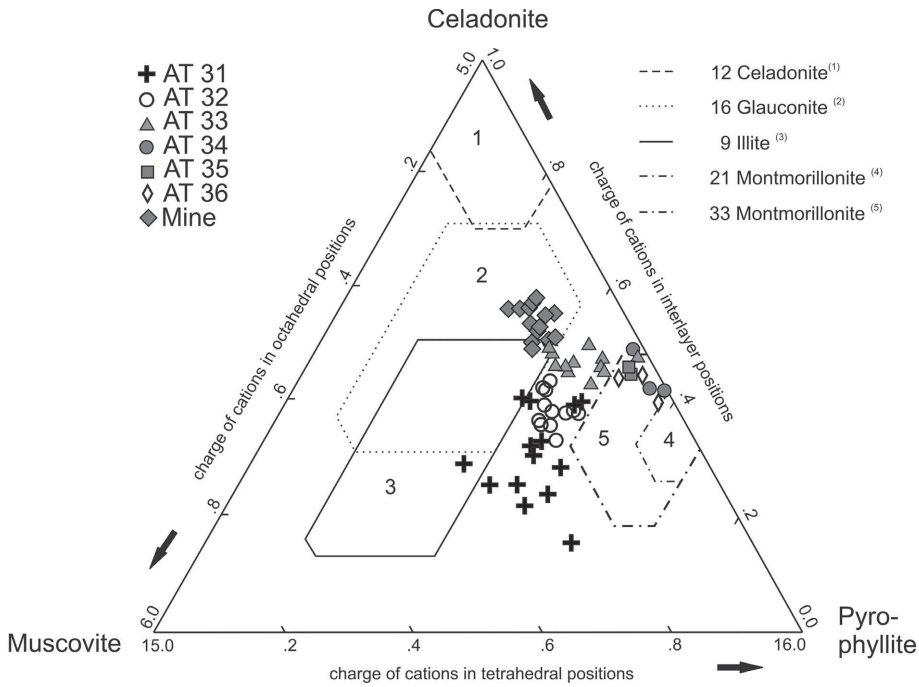

Figure 7. Charge-distribution diagram with end-members celadonite, muscovite, and pyrophyllite (modified from Köster, 1977). Samples AT31−AT36 were from the surface Layer 16 (weathered); the sample 'mine' was from the subsurface and so was fresh.

glauconites at the top of the surface layer were interpreted to have been caused by rain water percolating through the surface layer and leaching ions preferably at the top of the layer.

Weathering of glauconite is usually accelerated by oxidizing and mildly acidic conditions. Such weathering causes a loss of K and Fe and the crystallization of smectite (Ruffell *et al.*, 2003). Pyrite, if intimately associated with glauconite, oxidizes under surface conditions. This process enhances the weathering of glauconite because of the generation of acidic sulphate solutions (El-Sharkawi and Al-Awadi, 1982). Fe (oxyhydr)oxides form because of glauconite alteration (Meunier, 2004). Thin-section analyses revealed that the external boundaries of the glauconite became fuzzy and a greenish alteroplasma formed. The latter became increasingly brown as weathering intensified. The larger amount of matrix in the surface samples was possibly caused by alteration of glauconite grains to an argillaceous material.

Gypsum and anhydrite precipitate as a result of surface alteration. S is released by dissolution of pyrite. Jarosite forms at a pH of 3.5 by the reaction with sulfuric acid, which is also derived from pyrite dissolution. The greater S content in individual grains at the top of the layer can also be explained by a breakdown of pyrite; Fe ions were leached out and S was incorporated into the glauconite grains.

The decrease in weathering from the top to the bottom of Layer 16 was also documented in the clay mineralogy of the samples. The grains of the upper samples had a more smectitic composition; toward the base of the layer the grains were mixed-layer illite-smectite to illite minerals (Figure 7).

Comparison of surface and subsurface glauconite grains

Open-pit mining started in 1967, meaning that the maximum exposure time of the Abu Tartur glauconitic sandstones to surface-atmospheric conditions in an arid climate was 42 y until the time at which they were sampled. The summers in the Western Desert are hot and dry, the winters moderate; rainfall is episodic and spotty and amounts to 1−5 mm/y (Bornkamm and Kehl, 1989).

Compared to the surface samples, the glauconite grains of the fresh subsurface sample had a more intense color. The grains of the subsurface sample, representing fresh, unweathered grains, were light to intense dark green in color while surface samples showed greenish, yellowish to brownish glauconite grains under the microscope (Figure 4a,b), indicative of weathering. The color differences are related to the relative amount of Fe(II) and Fe(III) in the glauconite (Fanning *et al.*, 1989) and the formation of Fe (oxyhydr)oxides. The fresh sample contained fewer color-zoned grains and less matrix than the surface sample, because weathering had not yet affected the external boundaries of the grains.

Fe is an important redox indicator for weathering conditions (Fanning *et al.*, 1989).

Chemical analyses of glauconites in the literature show the structural Fe to be mainly Fe(III), typically only 10−15% of the Fe in glauconite analyses is

reported as Fe(II) (Odom, 1976; Fanning *et al.*, 1989). Fanning *et al.* (1989) studied the relative amounts of ferrous and ferric iron in the glauconites of the oxidized and reduced zones. Glauconite from the reduced zones contained more Fe(II) than the glauconite from the oxidized zones, suggesting that the oxidation state of the structural Fe does in part reflect the oxidation status of the material (Fanning *et al.*, 1989), which agrees with the FeO content of the Abu Tatur weathered (oxidized) surface samples with <1 wt.% FeO, whereas the fresh (reduced) subsurface samples had values of 2 wt.% FeO.

The maturity of glauconite predominantly reflects the residence time of the green grains at the sea bed before burial (Odin and Matter, 1981). The morphology and the K_2O content of the glauconite grains are good indicators of their maturity (Amorosi, 1995). Odin and Matter (1981) and Odin (1988) suggested four successive stages for glauconitization, which follow one after the other at the sediment-water interface as long as suitable conditions are present:

(1) The nascent stage corresponds to the first development of Fe-rich glauconitic minerals at the expense of detrital material. The K_2O content ranges between 2 and 4%. The first stage is strongly dependent on porosity and permeability which allows ion migration and chemical reactions.

(2) The slightly evolved stage is characterized by the near disappearance of detrital minerals and the presence of pores that are progressively filled with authigenic clays which contain between 4 and 6% K_2O.

(3) The evolved stage results from a series of successive recrystallizations and tends to obliterate the initial structure. The clay growth occurs preferentially and more rapidly in the central zone of the grains. This causes an increase in the initial volume and the formation of cracks in the outer zone. The K_2O content ranges from 6 to 8%.

(4) The highly evolved stage corresponds to the filling of cracks with authigenic minerals, resulting in smooth outlines of the granules. The K_2O content exceeds 8% of the total granule (Chamley, 1989).

In Abu Tartur, the weathering of the glauconite grains at surface prevents an exact determination of their maturity using morphology and K contents of the grains. Grains showing a morphology which would indicate an evolved stage (Odin and Matter, 1981) contained less K than expected for this stage of evolution. This can be interpreted as a weathering effect. The fresh subsurface sample was not affected by weathering. Accordingly, the evolutionary stage indicated by grain morphology and the K content were well correlated in the subsurface sample. Glauconite grains of the mine sample showed an evolved stage of evolution. Based on comparison with data by Odin and Matter (1981), the estimated duration of evolution was ~10^4 to 10^5 y for the subsurface sample.

The clay fraction of the fresh sample consisted of mixed-layer illite (glauconite)-smectite minerals richer in glauconitic layers (80%) than the surface samples (52%). Electron microprobe analyses also found that grains of the fresh sample contained larger amounts of K and Fe than grains from altered surface samples. Formula calculations from chemical analyses of single grains and subsequent plots in the charge-distribution diagram after Köster (1977) confirmed that the grains of the mine sample were pure glauconites (Figure 7). In the surface samples, K was leached out from the rock by percolating waters while the Fe left the glauconites to precipate as an independent Fe (oxyhydr)oxide phase (Meunier, 2004). The escape of K from the crystal lattice led to the formation of smectite.

Meunier (2004) described the weathering of glauconite as a progressive transformation into mixed-layer Fe-rich illite-smectite and eventually into smectites.

The data from thin-section analyses, electron microprobe analyses, and X-ray diffraction suggest strongly that the weathering sequence is a reversal of the sediment glauconitization (Hower, 1961; Velde, 1976).

The formation of glauconite is thus a reversible process at Earth-surface conditions (Meunier, 2004).

CONCLUSIONS

The clay fractions of the glauconitic sandstones from the surface and subsurface samples consist of randomly interstratified and ordered mixed-layer glauconite (illite)-smectite minerals, with more expandable smectite layers (50 %) in the weathered samples from the surface.

The muscovite-pyrophyllite-celadonite charge-distribution diagram shows for surface samples a clear weathering trend within Layer 16 from smectitic glauconite at the top to illitic glauconite at the bottom of the layer; the fresh subsurface sample plots exactly in the field for glauconite.

Surface samples are too altered for an exact determination of maturity using the K content and the grain morphology; they do not correlate. The morphology and the K content of the mine sample indicate an evolved stage of glauconitization.

The color, mineralogy, and chemistry show that the surface samples are strongly altered by weathering and that glauconite under surface conditions transforms progressively into Fe-rich mixed-layer illte-smectite and then into smectite.

For any valid chemical and mineralogical characterization and interpretation of glauconite at the surface, these weathering effects must be taken into consideration.

ACKNOWLEDGMENTS

Funding of the study was made possible by two scholarships provided by the University of Vienna to B.P. Special thanks to Wolfgang Hujer for his support and constructive remarks. The authors are indebted to Walter Strasser and Hannes Kugler from the Technische Prüfan-

stalt (TPA) for their help. The authors also benefited from helpful discussions with Emad Ramzy Philobbos of the University of Assiut. Many thanks to Mervat A. El Haddad from the University of Assiut and Ezzat A. Ahmed for their hospitality and to Peter Krois for valuable discussions which improved the manuscript. Christian Baal, Sigrid Hrabe, Claudia Beybel, and Franz Kiraly are acknowledged for their technical assistance and Norbert Irnberger, Erich Draganits, and Andrea Schicker for their help drawing the figures. Finally, the authors thank the reviewers for their efforts and their constructive comments from which the manuscript benefited greatly.

REFERENCES

Amorosi, A. (1995) Glauconite and sequence stratigraphy: a conceptual framework of distribution in siliciclastic sequences. *Journal of Sedimentary Research*, *B* **65**, 419–425.

Amorosi, A. (1997) Detecting compositional, spatial and temporal attributes of glauconite: a tool for provenance research. *Sedimentary Geology*, **109**, 135–153.

Bailey, S.W., Brindley, G.W., Kodama, H., and Martin, R.T. (1979) Report of The Clay Minerals Society Nomenclature Committee for 1977 and 1978. *Clays and Clay Minerals*, **27**, 238–239.

Bornhold, B.D. and Giresse, P. (1985) Glauconitic sediments on the continental shelf of Vancouver Island, British Columbia, Canada. *Journal of Sedimentary Petrology*, **55**, 653–664.

Bornkamm, R. and Kehl, H. (1989) Landscape ecology of the Western Desert of Egypt. *Journal of Arid Environments*, **17**, 271–277.

Brindley, G.W. and Brown, G. (1980) *Crystal Structures of Clay Minerals and their X-ray Identification*. Monograph **5**, Mineralogical Society, London, 495 pp.

Burst, J.F. (1958a) "Glauconite pellets": their mineral nature and applications to stratigraphic interpretations. *AAPG Bulletin*, **42**, 310–337.

Burst, J.F. (1958b) Mineral heterogeneity in glauconite pellets. *American Mineralogist*, **43**, 481–497.

Chamley, H. (1989) *Clay Sedimentology*. Springer, Berlin, Heidelberg, 623 pp.

Ehlmann, A., Hulings, N., and Glover, E. (1963) Stages of glauconite formation in modern foraminiferal sediments. *Journal of Sedimentary Petrology*, **33**, 87–96.

El-Sharkawi, M.A. and Al-Awadi, S.A. (1982) Alteration products of glauconite in Burgan oil field, Kuwait. *Journal of Sedimentary Petrology*, **52**, 999–1002.

Fanning, D.S., Rabenhorst, M.C., May, L., and Wagner, D.P. (1989) Oxidation state of iron in glauconite from oxidized and reduced zones of soil-geologic columns. *Clays and Clay Minerals*, **37**, 59–64.

Geptner, A.R. and Ivanovskaya, T.A. (2000) Glauconite from lower cretaceous marine terrigenous rocks of England: A concept of biochemogenic origin. *Lithology and Mineral Resources*, **35**, 5, 434–444.

Glenn, C.R. and Arthur, M.A. (1990) Anatomy and origin of a Cretaceous phosphorites-greensand giant, Egypt. *Sedimentology*, **37**, 123–154.

Hendriks, F., Luger, P., Kallenbach, H., and Schroeder, J.H. (1984) Stratigraphical and sedimentological framework of the Kharga-Sinn El-Kaddab stretch (western and southern part of the Nile Basin), Western Desert, Egypt. *Berliner geowissenschaftliche Abhandlungen* (A), **50**, 117–151.

Hower, J. (1961) Some factors concerning the nature and the origin of glauconite. *American Mineralogist*, **46**, 313–334.

Ireland, B.J., Curtis, C.D., and Whiteman, J.A. (1983) Compositional variation within some glauconites and illites and implications for their stability and origins. *Sedimentology*, **30**, 769–786.

Issawi, B. (1972) Review of Upper Cretaceous-Lower Tertiary Stratigraphy in central and southern Egypt. *AAPG Bulletin*, **56**, 8, 1448–1463.

Klitzsch, E., Harms, J.C., Lejal-Nicol, A., and List, F.K. (1979) Major subdivisions and depositional environments of Nubia strata, southwestern Egypt. *AAPG Bulletin*, **63**, 967–974.

Köster, H.M. (1977) Die Berechnung kristallchemischer Strukturformeln von 2:1-Schichtsilikaten unter der Berücksichtigung der gemessenen Zwischenschichtladungen und Kationenumtauschkapazitäten, sowie die Darstellung der Ladungsverteilung in der Struktur mittels Dreieckskoordinaten. *Clay Minerals*, **12**, 45–54.

Loveland, P.J. (1981) Weathering of a soil glauconite in southern England. *Geoderma*, **25**, 35–54.

Mansour, H.H. and Khallaf, A.F. (1979) Application of textural characteristics for depositional environment interpretation of the Upper Cretaceous-Paleocene east of Idfu-Sibaiya, Nile Valley. *Annals of the Geological Survey of Egypt*, **9**, 498–522.

Mansour, H.H., Youssef, M.M., and El Younsi, A.R. (1979) Petrology and sedimentology of the Upper Cretaceous, Paleocene succession northwest of Kharga Oasis, Egypt. *Annals of the Geological Survey of Egypt*, **9**, 471–497.

Marshall, C.E. (1949) The structural interpretation of chemical analyses of the clay minerals. In *The Colloid Chemistry of the Silicate Minerals*. Academic Press, New York, 159 pp.

Meunier, A. (2004) *Clays*. Springer, Berlin, 472 pp.

Meunier, A. and El Albani, A. (2007) The glauconite-Fe-illite-Fe-smectite problem: a critical review. *Terra Nova*, **19**, 95–104.

Moore, D.M. and Reynolds, R.C. Jr. (1997) X-*ray diffraction and the Identification and Analysis of Clay Minerals*. Oxford University Press, New York, 378 pp.

Notholt, A.J.G. (1985) Phosphorite resources in the Mediterranean (Tethyan) Phosphogenetic Province: A progress report. *Sciences Géologiques Memoire*, **77**, 9–21.

Odin, G.S. (1988) *Green Marine Clays*. *Developments in Sedimentology*, **45**, Elsevier, Oxford, UK, 445 pp.

Odin, G.S. and Matter, A. (1981) De glauconiarum origine. *Sedimentology*, **28**, 611–641.

Odom, E. (1976) Microstructure, mineralogy and chemistry of Cambrian glauconite pellets and glauconite, Central U.S.A. *Clays and Clay Minerals*, **24**, 232–238.

Pettijohn, F.J., Potter, P.E., and Siever, R. (1987) *Sand and Sandstone*. Springer, New York, 553 pp.

Ruffell, A.H., Worden, R.H., and Evans, R. (2003) Paleoclimate controls on spectral gamma-ray radiation from sandstones. *IAS Special Publication*, **34**, 93–108.

Said, R. (1962) *The Geology of Egypt*. Elsevier, New York, 377 pp.

Sediek, K.N. and Amer, A.M. (2001) Sedimentological and technological studies of Abu Tartur Black Shales, Western Desert, Egypt. *Physicochemical Problems of Mineral Processing*, **35**, 141–152.

Soliman, M.A., Habib, M.E., and Ahmed, E.A. (1986) Sedimentologic and tectonic evolution of the Upper Cretaceous–Lower Tertiary succession at Wadi Qena, Egypt. *Sedimentary Geology*, **46**, 111–133.

Strickler, M.E. and Ferrell, R.E. Jr (1990) Fe substitution for Al in glauconite with increasing diagenesis in the first Wilcox sandstone (Lower Eocene), Livingston Oasrish, Louisiana. *Clays and Clay Minerals*, **38**, 69–76.

Tantawy, A.A., Keller, G., Adatte, T., Stinnesbeck, W., Kassab A., and Schulte P. (2001) Maastrichtian to Paleocene depositional environment of the Dakhla Formation, Western Desert, Egypt: sedimentology, mineralogy, and

integrated micro- and macrofossil biostratigraphies. *Cretaceous Research*, **22**, 795–827.

Van Houten, F.B., Bhattacharyya, D.P., and Mansour, S.E.I. (1984) Cretaceous Nubia Formation and correlative deposits, eastern Egypt: Major regressive-transgressive complex. *Geological Society of America Bulletin*, **95**, 397–405.

Velde, B. (1976) The chemical evolution of glauconite pellets as seen by microprobe determinations. *Mineralogical Magazine*, **40**, 315, 753–760.

Ward, W.C. and McDonald, K.C. (1979) Nubia Formation of central eastern Desert, Egypt-Major subdivisions and depositional setting. *AAPG Bulletin*, **63**, 975–983.

Wassef, A.S. (1977) On the results of geological investigations and ore reserves calculations of Abu Tartur phosphorite deposits. *Annals of the Geological Survey of Egypt*, **9**, 1–60.

Wolff, R.G. (1967) X-ray and chemical study of weathering glauconite. *American Mineralogist*, **52**, 1129–1138.

(*Received 18 February 2011; revised 20 February 2012; Ms. 545; AE: L.B. Williams*)